Available online at www.sciencedirect.com
ScienceDirect
Trans. Nonferrous Met. Soc. China 35(2025) 2572−2585
Transactions of Nonferrous Metals Society of China
www.tnmsc.cn

Fabrication of Ti/Mg bimetal composite in Ti−6Al−4V pyramidal lattice structure via AZ91D melt infiltration

Yuan-bing WU[1], Jian-hua ZHAO[1,2,3], Chao WEI[1], Cheng GU[1,2,3], Ya-jun WANG[1,2,3]

1. College of Materials Science and Engineering, Chongqing University, Chongqing 400045, China;
2. National Engineering Research Center for Magnesium Alloys, Chongqing University, Chongqing 400044, China;
3. National Key Laboratory of Advanced Casting Technologies, Chongqing 400044, China

Received 18 December 2023; accepted 1 July 2024

Abstract: Titanium/magnesium alloy bimetal composites show promising prospects for lightweight applications. The Ti/Mg bimetal composite was fabricated in Ti−6Al−4V pyramidal lattice structure via AZ91D melt infiltration. Comparative analysis of the tensile and compressive properties was conducted between the composite and its constituent materials (Ti−6Al−4V lattice structure and AZ91D matrix). The tensile strength of the composite (95.9 MPa) was comparable to that of the Ti−6Al−4V lattice structure (94.4 MPa) but lower than that of the AZ91D alloy (120.8 MPa) due to gaps at the bimetal interfaces hindering load transfer during tension. The composite exhibited greater elongation (1.7%) compared to AZ91D (1.4%) alloy but less than the Ti−6Al−4V lattice structure (2.6%). The compressive performance of the composite outperformed that of the Ti−6Al−4V lattice structure, underscoring the significance of the AZ91D alloy in compressive deformation. Fracture analysis indicated that the predominant failure reasons in both the composite and lattice structures were attributed to the breakage of lattice struts at nodes caused by the stress concentration.

Key words: Ti−6Al−4V lattice structure; Ti−6Al−4V/AZ91D bimetal composite; melt infiltration; mechanical properties; fractography

1 Introduction

Comprising meticulously organized, three-dimensional formations, the open-cell lattice structure embodies a spatially ordered arrangement, crafted from recurring unit cells intricately connected by designated nodes [1]. The geometrical dimensions and configured shapes of these unit cells are precisely delineated by the strut elements constituting their framework. Due to their structural characteristics and unique properties, lattice structures are also known as lattice materials [2]. These materials have distinguished themselves by being lightweight, possessing high specific strength and surface area, excellent energy absorption efficiency, and customizable shapes and functionalities [1]. Lattice materials have already been adopted as lightweight components in the aerospace and automotive industries [3]. Many studies have demonstrated that the performance of lattice materials was significantly determined by the structure design, geometrical parameters, porosity [4], and manufacturing process parameters [5]. Selective laser melting (SLM) is an additive manufacturing method that provides a potential means for fabricating many complex structures that are unachievable using conventional manufacturing techniques [2]. This process manufactures metallic components from CAD data by gradually fusing metallic powders layer by layer in a “bottom-up” direction utilizing a high-powered laser beam source.

Corresponding author: Jian-hua ZHAO, Tel: +86-13508361677, E-mail: zjhwzf@sina.com
https://doi.org/10.1016/S1003-6326(25)66833-6

The metal matrix composites exhibit outstanding characteristics, including exceptional mechanical and thermal properties as well as remarkable corrosion resistance, making them ideal for many applications such as aerospace, marine, electronic packaging, and thermal management [6]. These composites, with different features, have been produced using various processing and approaches. For example, Mg/steel [7], and Mg/Fe [8] were produced by welding, Al/steel [9], and Mg/Al [10,11] were fabricated by compound casting, and another widely utilized method for fabricating metallic composites was compounding a continuous matrix phase with singular or multiple reinforced phases, typically used for the manufacture of short fiber and particle-reinforced composites [12]. However, the components of these composites prepared by traditional technologies are not mutually interpenetrated and discontinuous in 3D space. Recently, additive manufacturing processes using multiple materials have been developed for the production of composites. The metal deposition directly was used to prepare Ti/steel [13] and Ni/steel [14] composite from powdered materials; however, the resolution is somewhat limited, which restricts the use of this method for intricate geometries [15]. SLM technology is another additive manufacturing technique that can prepare composites with complex geometries and net-shaped objects. LIU et al [16] successfully manufactured laminates 316 steel/Cu bimetal with a metallurgical bond interface using SLM. MEI et al [17] also fabricated 316L stainless/Inconel 718 composite parts using SLM; however, some cracks and porosities were found at or near the interfaces. The relatively low production rates of this technique have also limited its widespread utilization.

Recently, an up-and-coming fabrication technology called printcasting has been proposed to improve productivity, which combines the SLM technique with a casting process to fabricate metallic composites [18]. This technology combines the advantages of the SLM technique to print the component with complex geometry and the benefits of a flexible casting process. Bimetal composites such as A356/steel composite [18,19] and Mg/NiTi interpenetrating phase composite [20] were successfully fabricated by this technology. These composites exhibit a unique microstructure characteristic as the matrix phase and reinforcement phase are continuous, three-dimensional, and mutually penetrating. This unique structure characteristic endows these composites with superior mechanical properties including lightweight, specific strength, considerable ductility, and exceptional energy absorption during hypervelocity impact. Therefore, they are attractive candidates for structural and functional materials [18−20].

Titanium alloys are known for their exceptional corrosion resistance, high specific strength, and impressive high-temperature stability (≤600 °C), making them valuable materials in industries such as aerospace, nuclear energy, and chemicals [21]. However, the high costs associated with smelting and processing titanium alloys have restricted their widespread use. The approach of combining titanium alloys with dissimilar metals to create bimetallic components has emerged as a popular and effective strategy for cost reduction. Examples of such combinations include Ti/Al [22] and Ti/Cu [23]. On the other hand, magnesium alloys offer advantages like low density, high specific strength, and ease of processing [24]. However, its broader application is hindered by factors such as low absolute strength, poor corrosion resistance, and poor high-temperature strength [25]. Titanium alloy and magnesium alloy have complementary advantages in terms of performance and economy. By combining titanium with magnesium alloys, it is possible to retain the specific characteristics of each while overcoming the shortcomings of individual materials, thereby achieving a dual complementary goal of performance and economy. However, the significant disparity in metallurgical reactions and extreme incompatibility between Mg and Ti is a substantial obstacle to producing their composites using conventional methods.

Printcasting technology is a new process for fabricating bimetal composite materials. However, no research has been conducted on the preparation of Ti/Mg composite materials utilizing printcasting technology. As a result, this study aims to investigate the performance of Ti/Mg bimetal composite prepared by printcasting technology. This process involved constructing Ti lattice structures that were composed of pyramidal unit cells using SLM technology. The cavities within these structures were then infiltrated with molten

magnesium alloy. The produced materials were investigated in terms of their microstructure, tensile and compressive properties, as well as fracture behavior. This investigation not only expanded the preparation technique for Ti/Mg composite materials but also offered valuable insights applicable to the development of other bimetal composites featuring significant disparities in physical and chemical attributes, weak reactivity, and low mutual solubility.

2 Experimental

2.1 SLM process

In the SLM process, feedstock material consisting of Ti−6Al−4V alloy powders was utilized, which were atomized using argon and ranged in size from 15 to 52 μm. Table 1 shows the chemical composition of the powder. A commercial SLM machine (BLT-S210, Xi'an, China) was used to fabricate the lattice structure parts. The SLM parameters for the SLM-fabricated Ti−6Al−4V in Ref. [26] were employed, including a laser power of 157 W, a layer thickness of 50 μm, a scan speed of 225 mm/s, and a hatch spacing of 100 μm.

Figure 1(a) depicts the geometrical parameters of the lattice structure with a porosity of 86.1% (relative volume fraction of 13.9%). Our previous study [26] provided a more comprehensive description of the parameter design process. The parts used for compressive and tensile testing are shown in Fig. 1(b) and Fig. 1(c), respectively. The side length of the compressive cube sample (Fig. 1(b)) was 10.6 mm. The nonstandard tensile specimen with a gauge length (L) of 45 mm was shown in Fig. 1(c). To avert stress concentration-induced failures, rounded corners were included at the junctions of the solid zones and lattice zones as illustrated in Fig. 1(c).

2.2 Casting process

The AZ91D alloy, known for its high specific strength, good electromagnetic shielding performance, and especially excellent casting performance, is an extensively utilized cast magnesium alloy material [24]. Table 2 lists the composition of the AZ91D alloy employed in this study.

The AZ91D ingots were melted in a stainless steel crucible within an electrical resistance furnace at a high temperature of 750 °C while being shielded by a combination of CO_2 and 0.5 vol.% SF_6. After degreasing in an alkali cleaner and acid washing (30 vol.% hydrofluoric acid and 70 vol.% nitric acid, 30 s), Ti−6Al−4V lattice structures were placed in a preheated steel mold at 350 °C to be ready for pouring. Then, the molten AZ91D melt was poured steadily into the tailored mold. To

Table 1 Chemical composition of Ti−6Al−4V powder (wt.%)

Al	V	O	Fe	C	H	N	Cu	Sn	Ti
6.38	3.93	0.17	0.27	0.013	0.003	0.0072	0.091	0.01	Bal.

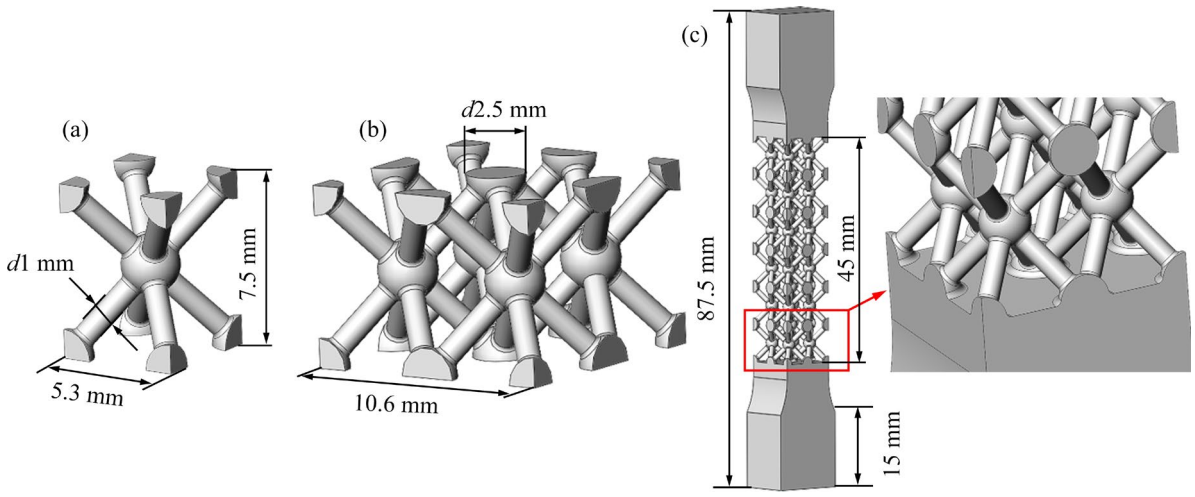

Fig. 1 (a) Unit cell dimensions of pyramidal lattice structure; (b, c) Compressive and tensile testing specimens with pyramidal lattice structure fabricated by SLM, respectively

Table 2 Chemical composition of AZ91D ingot (wt.%)

Al	Zn	Fe	Ni	Mn	Cu	Mg
9.580	0.6530	0.0017	0.0001	0.2194	0.0021	Bal.

guarantee that there is adequate contact between the AZ91D melt and the Ti−6Al−4V lattice structure, the mold was kept tightly closed until the AZ91D melt was fully solidified and cooled to room temperature. Wire-cutting was then employed to cut standard tensile samples from the ingot. For clearer elucidation of the properties and microstructure of the bimetal, the as-cast AZ91D magnesium components were cast using identical conditions for comparison.

2.3 Characterization

The metallographic samples for microstructure analysis were cut from the bimetal ingot through wire-cutting. The samples were ground using silicon carbide (SiC) paper and polished with a 0.5 μm Al_2O_3 solution. The samples were etched using a solution comprising 4 vol.% concentrated nitric acid and 96 vol.% ethyl alcohol. The microstructural observation and fractographic analyses were performed using a scanning electron microscope (SEM, TESCAN VEGAN−3 LMH) with an energy dispersive spectrometer (EDS).

Tensile and compressive tests were conducted on the specimens (Ti−6Al−4V lattice structure, as-cast AZ91D alloy, and Ti−6Al−4V AZ91D bimetal) depicted in Fig. 2, under uniaxial loading

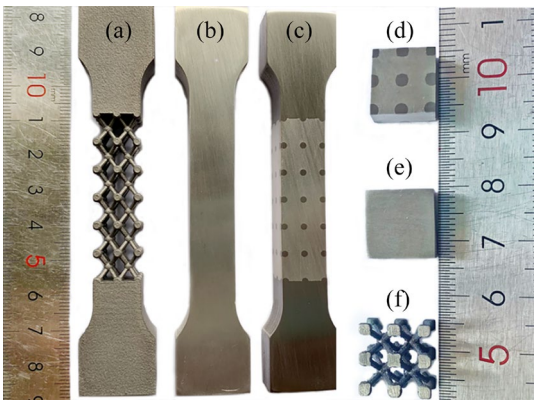

Fig. 2 Images of experimental specimens: (a) Ti−6Al−4V lattice structure dog-bone; (b) As-cast AZ91D dog-bone; (c) Ti−6Al−4V/AZ91D bimetal composite dog-bone; (d) Bimetal composite cube; (e) As-cast AZ91D cube; (f) Ti−6Al−4V lattice structure cube (The dog-bones and cubes were utilized for tensile and compressive tests, respectively)

conditions at room temperature. Tensile specimens underwent mechanical grinding and polishing to achieve a surface finish of approximately 10 μm. To minimize experimental error, three samples were tested for each material. The testing was performed in displacement-controlled mode by utilizing a servo-hydraulic mechanical testing system (CMT−6305-300 kN). The speed was 1 mm/min for both tensile and compressive tests. An extensometer was employed to measure the elongation during the tensile testing. The effective cross-sectional area (35.2 mm^2) [27] of dog-bone-shaped tensile lattice structure was utilized to calculate the UTS.

3 Results and discussion

3.1 Microstructural characteristics

In this study, the ability of the AZ91D melt to fully infiltrate the cavity of the lattice structure is critical for the production of Ti−6Al−4V/AZ91D bimetal composite through the current casting process. Utilizing the same casting process, as well as identical geometrical parameters and gap size between the lattice structure roots depicted in Fig. 1(a), Ti−6Al−4V/AZ91D bimetal composite was fabricated, with the filling quality characterized using AZ91D alloy as an index. Figure 3 shows SEM micrographs from the cross-section and interface of the bimetal composite at different magnifications. It can be seen from the low-magnification SEM image of the cross-section (Fig. 3(a)) that the substrate of the Ti−6Al−4V lattice structure is tightly bound to the AZ91D alloy, and no discernible void or gap is evident in the bimetal joint. The results indicate the AZ91D alloy melt is embedded well into the cavity of the Ti−6Al−4V lattice structure during the present casting process.

It can be found that the interface's macroscopic morphology is uneven in Fig. 3(b) when compared to the interface of rolled Ti−6Al−4V/AZ91D bimetal [28]. This is because during the SLM procedures, the Ti−6Al−4V lattice structure surface was oxidized, and partially melted particles were attached to it, resulting in a coarse surface [4]. Meanwhile, the jagged interface created by this inevitable imperfection can enhance the mechanical bonding of the Ti−6Al−4V/AZ91D interface. Several holes and a continuous gap with a maximum width of about 2 μm are discernible at

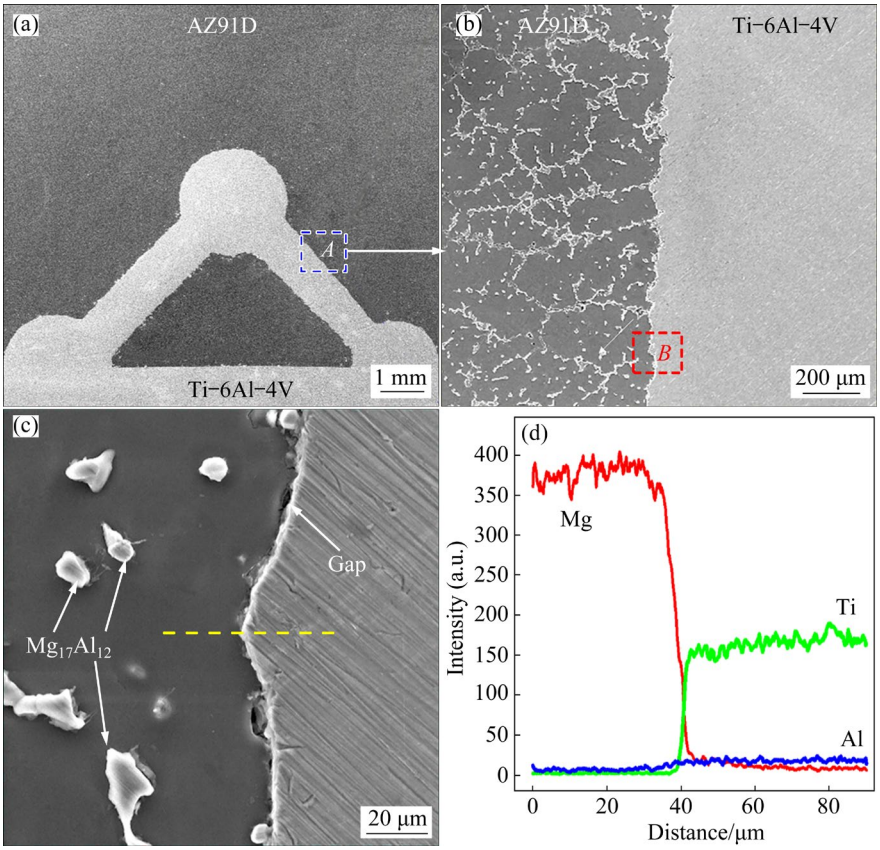

Fig. 3 SEM images and EDS line scan results of bimetal composite interface: (a) Low-magnification image; (b) Magnified view of Region *A* in (a); (c) Magnified view of Region *B* in (b); (d) EDS line scan results across interface marked in (c)

the interface. Three reasons could explain the formation of the gap and holes. Firstly, due to the immiscibility characteristics of Mg and Ti, no metallurgical reaction products are formed between them during the melting and solidification process. Secondly, the surface of lattice structure is rapidly oxidized before contacting liquid AZ91D melt, resulting in poor wettability between Ti−6Al−4V and AZ91D; hence, the liquid phase metal and the solid phase metal surface cannot be closely touched. Other studies have also reported the occurrence of gap formation at the Ti−6Al−4V/ AZ91D interface [28]. Figure 3(d) exhibits the EDS line scanning spectrum captured along the yellow dotted line highlighted in Fig. 3(c), providing compelling evidence that no diffusion reaction layer or metallurgical reaction product exists at the interface. According to the Mg−Ti binary phase diagram [29], Mg and Ti lack metallurgical compatibility, and their mutual solid solubility is very low. The maximum solid solubility of Mg in Ti is 0.9 at.% and that of Ti in Mg is 0.02 at.%. Mg and Ti cannot react to yield a secondary phase [30]. The positive enthalpy of the formation of the Mg−Ti binary compound further supports the lack of reaction at the interface [28].

The EDS elemental maps of the bimetal interface shown in Fig. 4 reveal the absence of any intermetallic compounds at the interface. The formation and distribution of Al−Ti compounds at the Ti−6Al−4V/AZ91D interfaces are dependent on the temperature and pressure, as indicated by the Al−Ti binary phase diagram [31], which shows that when the Al element in the AZ91D alloy reacts with Ti, such compounds can be formed. YAO et al [30] reported the presence of Al_3Mn nanophase, $Mg_{17}Al_{12}$, and $Al_3Ti + Ti_3Al$ duplex structure intermetallics in the vacuum diffusion bonding AZ91/TA2 bimetal. The $Mg_{17}Al_{12}$ intermetallics were also observed in the Ti−6Al−4V/AZ31B bimetal fusion zone fabricated by laser keyhole welding [32]. This shows that the Al element is accumulated at the AZ91D alloy grain boundaries, whereas the distribution of both Al and V in the

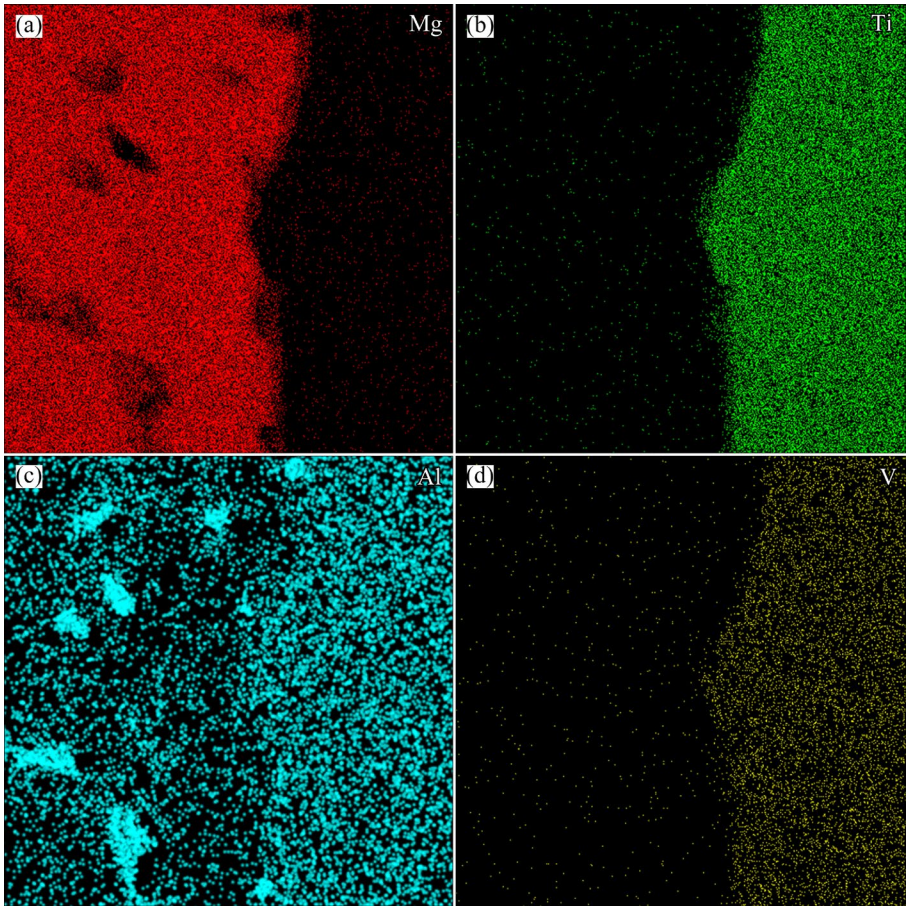

Fig. 4 EDS elemental distribution maps corresponding to Ti−6Al−4V/AZ91D bimetal composite interface in Fig. 3(c): (a) Mg; (b) Ti; (c) Al; (d) V

Ti−6Al−4V alloy is uniform. This is because the rapid solidification rate of the SLM process prevents the separation of alloying elements [33].

3.2 Tensile performance

Figure 5 depicts the quasistatic tensile stress−strain curves for all experimental materials investigated in this study. The related tensile properties, including elastic modulus (*E*), yield strength (YS), ultimate tensile strength (UTS), and elongation to fracture are listed in Table 3. The as-cast AZ91D alloy exhibits significantly higher elastic modulus but with an exceptionally lower elongation than Ti−6Al−4V lattice structure and Ti−6Al−4V/AZ91D bimetal. The UTS and YS of Ti−6Al−4V/AZ91D bimetal are commensurate with those of Ti−6Al−4V lattice structure and as-cast AZ91D alloy, respectively. Both the elastic modulus and elongation of Ti−6Al−4V/AZ91D bimetal are between those of the Ti−6Al−4V lattice structure and as-cast AZ91D alloy. This indicates that the elastoplastic deformation of the infiltrated lattice

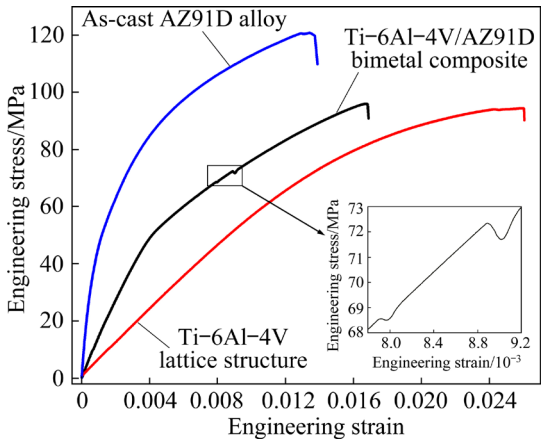

Fig. 5 Representative tensile stress−strain curves for all experimental materials

structure is affected by the AZ91D alloy matrix during tensile deformation, though it does not significantly impact the failure strength. ZHANG et al [35] reported that the mechanical properties of the Ti−6Al−4V lattice structure remained largely unaffected by the casting process, with similar microstructural and mechanical characteristics

observed before and after the casting.

Table 3 shows that the YS, UTS, and elongation of the current Ti−6Al−4V lattice structure with a porosity of 86.1% are 77.9 MPa, 94.4 MPa, and 2.6%, respectively. According to the reports in Ref. [36], the UTS and elongation for a Ti−6Al−4V diamond lattice structure with an 81.5% porosity were 62.5 MPa and 5.7%, respectively. The full dense Ti−6Al−4V manufactured through SLM demonstrates the YS of 978 MPa and UTS of 1143 MPa [34]. It is anticipated that the lattice structure of Ti−6Al−4V with a porosity of 86.1% should exhibit the YS of 136 MPa and UTS of 159 MPa. These predicted values are 43% and 41% greater than the values experimentally measured in this study. The observed difference between the predicted values and the experimental results is not unexpected and can be attributed to several factors. Firstly, despite using SLM process parameters consistent with those in Ref. [34], the "staircase effect" is more pronounced when fabricating lattice structures with inclined angles using SLM. This can affect dimensional accuracy, surface quality, and the presence of defects such as voids and unmelted particles, ultimately impacting the strength of the structures [1]. Secondly, the connections between struts at nodes can lead to stress concentration, which may result in a significant reduction in strength during the tensile process. Finally, the Ti−6Al−4V lattice structure in this study was annealed at 800 °C for 2 h, which may also be the reason for the reduced strength. The research shows that the SLMed Ti−6Al−4V primarily consists of needle-like α' martensite, which transforms into $\alpha+\beta$ phases after heat treatment, resulting in the increased ductility [37]. However, an increase in metal ductility often leads to a compromise in tensile strength, following the strength−ductility trade-off [38]. For example, LIU et al [37] conducted a study on SLM-fabricated Ti−6Al−4V alloy and reported a reduction of 16% in YS and 17% in UTS upon annealing. Similarly, CAO et al [39] observed a decrease of 13% in YS and 9% in UTS. They attributed the decrease in YS and UTS of the annealed Ti−6Al−4V alloy to the phase transformation from α' martensite to $\alpha+\beta$, and found that the α grain size increased as well as the lamellae become thicker compared to the as-built Ti−6Al−4V alloy.

From Table 3, the mechanical properties of as-cast AZ91D alloy obtained in this study are not much different from those reported in Ref. [40] under the condition of mechanical vibration with low frequency. The elastic modulus of the as-cast AZ91D alloy is 49.5 GPa in the present study, which is comparable with 46 GPa reported in Ref. [41]. The Ti−6Al−4V lattice structure with a porosity of 86.1% was found to have an elastic modulus of 6.4 GPa. In contrast, a Ti−6Al−4V lattice structure with a porosity of 18.5% was found to have an elastic modulus of 3.7 GPa, as reported by DOROSZKO et al [36].

Additionally, from Fig. 5, it can be seen that the tensile stress−strain curve of the composite exhibits discontinuity, as highlighted in the magnified section within the yellow outlined box in the inset. In the study conducted by CHENG et al [18], digital image correlation (DIC) coupled with finite element (FE) modeling was utilized to investigate the tensile damage process of 316/A356 composite material. The stress−strain curves of all samples exhibited considerable serrations, which were attributed to consecutive local fracture events within the samples, such as breakage of struts, coalescence of multiple cracks, and debonding events. The Ti−6Al−4V/AZ91D bimetal with the porosity of 86.1% (relative volume fraction of 13.9%) exhibits the elastic modulus of 13.9 GPa, UTS of 95.9 MPa, and elongation of 1.7%. It was reported that the AZ91D alloy reinforced with Ti−6Al−4V particles at a volume fraction of 20% exhibited higher UTS of 160 MPa but a lower

Table 3 Comparison of tensile properties of materials

Material	Elastic modulus/GPa	Yield strength/ MPa	Ultimate tensile strength/MPa	Elongation/%
Bulk Ti−6Al−4V(SLM) [34]	115±6	978±5	1143±6	11.8±0.5
Ti−6Al−4V lattice structure	6.4±0.21	77.9±0.14	94.4±0.1	2.6±0.2
Ti−6Al−4V/AZ91D composite	13.9±0.12	64.6±0.8	95.9±0.2	1.7±0.1
As-cast AZ91D	49.5±3.2	79.3±0.7	120.8±0.1	1.3±0.4

elongation of 0.5% compared to the AZ91D alloy. Additionally, the reinforced alloy demonstrated a higher elastic modulus of 70 GPa [42]. Research has demonstrated that incorporating interfacial products into the matrix can enhance the YS and increase the UTS of the composite [42]. Research by WEN et al [28] demonstrated that by preparing Ni and Cu coatings on the Ti−6Al−4V surface before bonding with AZ91D, a metallurgical bonding interface can be achieved, significantly enhancing the bonding strength of TC4/AZ91D bimetal. Future studies could focus on enhancing the tensile strength of TC4/AZ91D bimetal by creating metallurgical interfaces through coating preparation.

3.3 Compressive behavior

Figure 6 depicts the stress−strain curves for all the experimental materials subjected to compressive testing. It indicates that the as-cast AZ91D alloy exhibits higher yield stress and compressive strength compared to the composite and Ti−6Al−4V lattice structure. The presence of voids and gaps in the microstructure of the bimetal interface can be held responsible for this observation. The Ti−6Al−4V lattice structure exhibits the minimum yield stress and compressive strength. This contrasts with the tensile behavior where the UTS values of both Ti−6Al−4V lattice structure and bimetal are nearly identical. The gaps along with the interface of the composite were eliminated when subjected to compressive loading, while they grew larger during tensile loading. Consequently, the AZ91D alloy is vital to the compressive deformation of the

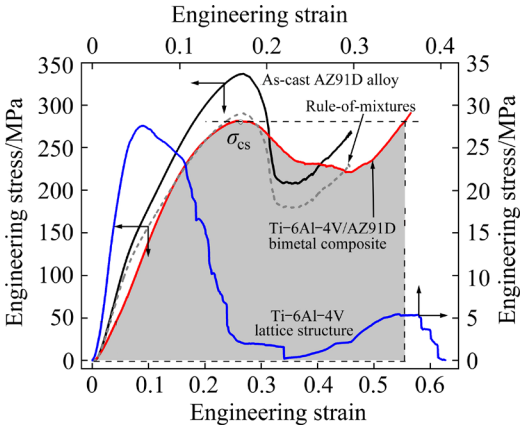

Fig. 6 Compressive engineering stress−strain curves for all experimental materials (σ_{cs} is the peak stress at the plateau stage)

Ti−6Al−4V/AZ91D bimetal. The imperfect bonding interface leads to the difference in tensile and compressive behavior between composite and reinforced scaffolds [19].

The weak interfaces between the Ti−6Al−4V lattice structure and AZ91D alloy, which tend to produce easy sliding, may also be responsible for the low elastic modulus of the bimetal. A similar phenomenon was also found in Mg/Fe [43] and Al/Fe bimetals [19]. The fact remains that the Ti−6Al−4V lattice structure plays a relatively insignificant role in the bimetal flow stress as it can accommodate substantial plastic deformation even when subjected to low levels of external stresses [44]. It can also be demonstrated that the compressive stress−strain curve of the composite does not exhibit multiple peaks analogous to the lattice structure's curve. For the pyramidal Ti−6Al−4V lattice structure with a porosity of 86.1%, the compressive elastic modulus and compressive strength were found to be 0.8 GPa and 27.6 MPa, respectively. A diamond-shaped Ti−6Al−4V lattice structure with a porosity of 80.8% was found to exhibit a compressive elastic modulus of 0.9 GPa and a compressive strength of 21 MPa [45]. Moreover, JIN et al [46] measured the compressive elastic modulus and compressive strength for the Ti−6Al−4V pyramidal lattice structure with a porosity of 83%, and the results were 0.55 GPa and 24.7 MPa, respectively.

It can also be found that the compressive stress−strain curve of the Ti−6Al−4V lattice structure demonstrates noticeable stress dips and the absence of plateaus. The stress−strain curve shows that the struts flex before the curves reach their first peak, with the middle two-layer struts experiencing the most bending. The stress concentration first occurs at the nodes where the junction connects to struts. Subsequently, the continuous compressive loading and collapse of rods result in the curves declining along with fluctuations. An analogous curve pattern was also found in a study of cubic and pyramidal Ti−6Al−4V lattice structure by CHOY et al [4] and YAO et al [47], respectively. During the quasi-static compressive test, the load-bearing capacity of the specimen increases rapidly once the first and second layers become aligned. As the material is compressed, the stress continues to rise. The energy absorption capability was determined from the area

under the stress−strain curve using the trapezoidal rule [4]. The energy absorption capacity of the pyramidal lattice structure with a porosity of 86.1% in this study is 3.5 MJ/m^3 (35% strain), which is comparable to that (3.94 MJ/m^3) of the cubic lattice structure with a porosity of 86.7 % [4].

To provide a comparison, the approximations based on the rule-of-mixtures [20] are shown as dash curves in Fig. 6. The stress in the composite at a particular strain, σ_{ROM}, was estimated by adding the stress in the Ti−6Al−4V lattice structure at the same strain to the stress in the AZ91D alloy, σ_{AZ91D}, weighted by its volume fraction, V_{AZ91D}, following the relationship of $\sigma_{ROM}=\sigma_{AZ91D}V_{AZ91D}+\sigma_{Ti-6Al-4V}\cdot V_{Ti-6Al-4V}$. The composite shows lower yield stress and lower compressive strength than σ_{ROM}. This discrepancy can be explained by the existence of an imperfect bonding interface with gaps, as seen in Fig. 3. The bimetal exhibits a noticeable feature where it maintains a relatively stable stress plateau beyond a strain of 0.55, following yielding but preceding the subsequent stress increase. This behavior is frequently observed in porous materials and suggests significant potential for energy absorption [48]. To determine the energy absorption capacity in the presence of a stable stress plateau, the area beneath the stress−strain curve was calculated before the stress reached the level of peak stress at the plateau stage (σ_{cs}) [29], as the shaded region shown in Fig. 6. For the Ti−6Al−4V/AZ91D bimetal in this study, the energy absorption capacity is 115.9 MJ/m^3, which is 17.8 MJ/m^3 lower than that of the Mg/Ni−Ti composite material with a NiTi volume fraction of 35.9% under the same strain rate (1×10^{-2} s^{-1}) and at room temperature [20]. On the other hand, it is higher than that of AZ91D and Ti−6Al−4V lattice structure by 12.8 and 112.4 MJ/m^3, respectively.

3.4 Fracture behavior

The macroscopic morphologies of fracture surfaces of all experimental materials after tensile testing are shown in Fig. 7. As seen, the fracture section of the Ti−6Al−4V lattice structure is inclined at an approximate angle of 45° to the load direction. The failure occurs in the gauge zone of the lattice structure rather than the region of the lattice structure connected to the entity, indicating that the addition of fillets is beneficial (Fig. 1(c)). The stress concentrations at the nodes are responsible for the fracture of lattice struts. Breakage at nodes was prevalent in lattice structures such as SLM-fabricated stainless steel lattice structure [49] and AlSi10Mg lattice structure [50]. For the as-cast AZ91D alloy, the failure mode shows the characteristics of brittle fracture, whose fracture morphology is relatively flush and perpendicular to the stretching direction (Fig. 7(b)), and the breakage of the sample occurs within the gauging zone.

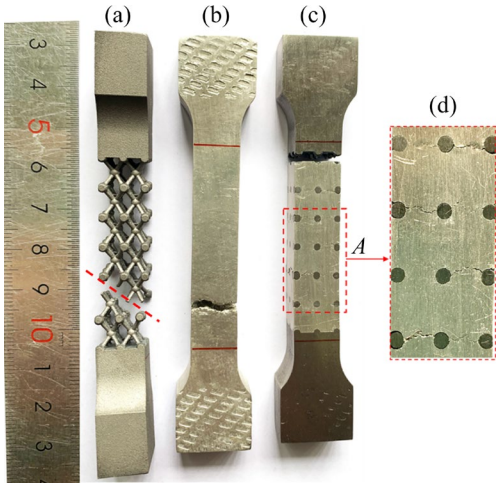

Fig. 7 Macroscopic morphologies of experimental samples after tensile tests: (a) Ti−6Al−4V lattice structure; (b) As-cast AZ91D alloy; (c) Ti−6Al−4V/AZ911 bimetal composite; (d) Magnified view of Region *A* in (c)

For the Ti−6Al−4V/AZ91D bimetal (Fig. 7(c)), the failure occurs at the end of the lattice structure. CHENG et al [18] used finite element analysis to simulate the tensile failure process of 316L lattice/A356 composite materials, indicating that under tensile load, the A356 matrix first detached from the 316 L lattice structure. Further loading induced local rotation and bending of lattice struts, causing stress concentration near the strut and lattice node junction. The lattice structure with a lower volume fraction (30%) exhibited higher stress concentration compared to the structure with a higher volume fraction (50%). Therefore, the low volume fraction (13.9%) of the Ti−6Al−4V lattice structure with a small-size strut was unable to compensate for the stress concentration, leading to localized deformation and ultimately leading to a localized failure at the strut−node junction. The approximate tensile strength of lattice structure and Ti−6Al−4V/AZ91D bimetal (Fig. 5) is attributed to the fact that both exhibit strut fracture as their dominant failure mode. The difference is that the

fracture location of struts is changed. Figure 7(d) depicts the presence of multiple cracks that are perpendicular to the tensile direction, as observed upon magnifying the marked region in Fig. 7(c). The cracking is mainly concentrated within the weaker AZ91D material and at the interfaces of the composite. To enhance the performance of composite materials with a low Ti−6Al−4V volume fraction, optimizing the local lattice structure can be done without changing the overall volume fraction. For example, introducing fillets between the struts and nodes to reduce constraints could provide additional benefits in energy absorption. Another potential modification is to design lattice struts with a gradient in thickness between nodes, increasing the cross-sectional area towards the node and decreasing the area between nodes.

To further identify the failure characteristics, the micromorphologies of all the fracture surfaces were observed by SEM. Figures 8(a−c) show the images of the Ti−6Al−4V lattice structure failure surface at three magnifications, demonstrating that the lattice structure breaks where the highest amount of stress is concentrated at the junction of the strut elements and nodes (as illustrated in Fig. 8(a)). However, the resistance to failure is mostly determined by strut diameter while the node size has little impact on the strength of the lattice

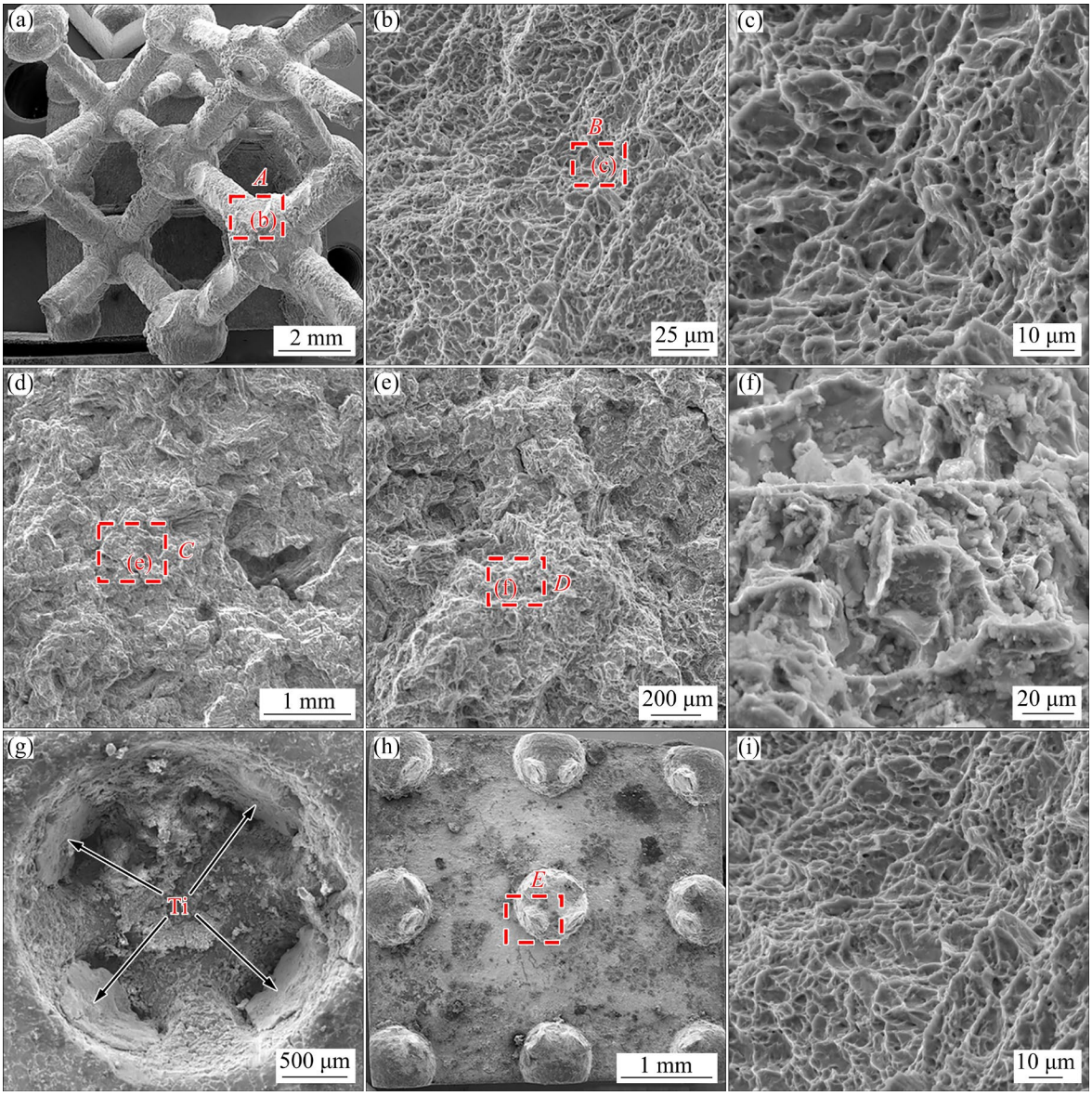

Fig. 8 SEM images of fracture surfaces after tensile tests: (a−c) Fracture surface of Ti−6Al−4V lattice structure; (d−f) Fracture surface of as-cast AZ91D; (g, h) Fracture surface of bimetal composite on sides of as-cast AZ91D and Ti−6Al−4V lattice, respectively; (i) Magnified view of Region *E* in (h)

structure [44]. The fracture surfaces exhibit considerable irregularity, also known as the areas of the fibrous fracture under low magnification (Fig. 8(b)). A ductile fracture can be confirmed in Fig. 8(c), where multiple tiny dimples and micro-cracks features without cleavage facets can be observed. The growth and coalescence of these defects result in lattice structure breakage during the tensile process.

The brittle failure of as-cast AZ91D alloy was further confirmed with the fracture morphology in Figs. 8(d−f). Due to the limited slip systems during the tensile process, the principal fracture modes are multiple microvoids, microcracks, and cleavage facets, as depicted in Fig. 8(d) and Fig. 8(f). Figure 8(f) displays a typical intergranular fracture with coarse dimples. The high hardness and brittleness of as-cast AZ91D alloy make the non-uniformly distributed $Mg_{17}Al_{12}$ phase accountable for the fracture [51]. The aforementioned brittle fracture characteristic elucidates the comparatively low elongation (1.3%) as depicted in Fig. 5 and Table 3.

Figures 8(g−i) show the fracture micrographs of Ti−6Al−4V/AZ91D bimetal composite at various magnifications. As seen in Fig. 8(g) and Fig. 8(h), the composite failure is the breakage of the struts located in the transition nodes. It is a result of the AZ91D matrix detached from the surface of the Ti−6Al−4V and interacting with the lattice struts during the tensile process. One more reason for that is the macroscopic jagged interface (see Fig. 3(b)) would increase the friction between the two components during the tensile process. In Fig. 8(i), the round pores surrounded by shallow dimples can be observed. The ultrafine lamellar α+β structure of SLM-manufactured Ti−6Al−4V alloys also demonstrates minuscule and deep dimple features [52]. Thus, the failure modes of the lattice structure before and after infiltration are ductile fractures. The failure mode of the Ti−6Al−4V/AZ91D bimetal is dominated by the Ti−6Al−4V lattice structure reinforcement, in which tensile strength significantly depends on the features of lattice structure.

4 Conclusions

(1) SEM observations and EDS analysis of the Ti−6Al−4V/AZ91D bimetal interface revealed the presence of gaps and no metallurgical products were generated. The alloying elements are distributed uniformly in the SLM-fabricated Ti−6Al−4V lattice structure but are found to be segregated at grain boundaries in the as-cast AZ91D alloy.

(2) The gaps at the interface hinder the stress transfer during the tensile process, resulting in the tensile strength of the composite material comparable to that of the lattice structure. The AZ91D alloy exhibited higher elastic modulus, yield stress, and ultimate tensile strength but a lower elongation than the Ti−6Al−4V lattice structure and bimetal composite materials.

(3) Compared to the lattice structure, the bimetal composite exhibits notably higher compressive properties and energy absorption capacity, indicating the indispensable contribution of the embedded AZ91D alloy in the compressive deformation process.

(4) The tensile failure modes of both the lattice structure and composite are determined to be the ductile fractures of struts positioned in the node, but the location of the fracture varies. In the case of the as-cast AZ91D alloy, the failure mode is found to be brittle.

CRediT authorship contribution statement

Yuan-bing WU: Methodology, Formal analysis, Investigation, Writing − Original draft; **Jian-hua ZHAO:** Resources, Funding acquisition, Supervision; **Chao WEI:** Methodology, Data curation; **Cheng GU:** Formal analysis, Writing − Review & editing; **Ya-jun WANG:** Formal analysis, Methodology.

Declaration of competing interest

The authors declare that they have no known competing financial interests or personal relationships that could have appeared to influence the work reported in this paper.

Acknowledgments

The authors acknowledge the financial support from the National Natural Science Foundation of China (Nos. 51875062, 52205336).

References

[1] MACONACHIE T, LEARY M, LOZANOVSKI B, ZHANG X Z, QIAN M, FARUQUE O, BRANDT M. SLM lattice structures: Properties, performance, applications and challenges [J]. Materials & Design, 2019, 183: 108137.

[2] ZHANG Xue-qin, ZHANG Ke-qiang, ZHANG Lu, WANG Wen-qing, LI Ying, HE Ru-jie. Additive manufacturing of cellular ceramic structures: From structure to structure–function integration [J]. Materials & Design, 2022, 215: 110470.

[3] SMEETS B J R, FAGAN E M, MATTHEWS K, TELFORD R, MURRAY B R, PAVLOV L, WEAFER B, MEIER P, GOGGINS J. Structural testing of a shear web attachment point on a composite lattice cylinder for aerospace applications [J]. Composites (Part B): Engineering, 2021, 212: 108691.

[4] CHOY S Y, SUN C N, LEONG K F, WEI J. Compressive properties of Ti−6Al−4V lattice structures fabricated by selective laser melting: Design, orientation and density [J]. Additive Manufacturing, 2017, 16: 213−224.

[5] MEZZETTA J, CHOI J P, MILLIGAN J, DANOVITCH J, CHEKIR N, BOIS-BROCHU A, ZHAO Y F, BROCHU M. Microstructure−properties relationships of Ti−6Al−4V parts fabricated by selective laser melting [J]. International Journal of Precision Engineering and Manufacturing-Green Technology, 2018, 5(5): 605−612.

[6] VIJAYA RAMNATH B, PARSWAJINAN C, DHARMASEELAN R, THILEEPAN K, NITHIN KRISHNA K. A review on aluminium metal matrix composites [J]. Materials Today: Proceedings, 2021, 46: 4341−4343.

[7] TAO Tao, LIU Jin-shui, ZHOU Dian-wu, LI Hui-ming, WANG Xin-yu. Microstructure and properties of magnesium/steel dissimilar metals by interlayer assisted laser welding [J]. Transactions of Nonferrous Metals Society of China, 2023, 33(3): 765−776.

[8] LI Tao-tao, BI Xiao-lin, LI Rui-feng. A strategy for bonding immiscible Mg/steel by laser-TIG butt fusion welding and lattice distortion on the Fe/Mg interface matching [J]. Materials & Design, 2022, 219: 110763.

[9] VENDRA L J, RABIEI A. A study on aluminum–steel composite metal foam processed by casting [J]. Materials Science and Engineering: A, 2007, 465(1/2): 59−67.

[10] LI Guang-yu, JIANG Wen-ming, GUAN Feng, ZHANG Zheng, WANG Jun-long, YU Yang, FAN Zi-tian. Preparation, interfacial regulation and strengthening of Mg/Al bimetal fabricated by compound casting: A review [J]. Journal of Magnesium and Alloys, 2023, 11(9): 3059−3098.

[11] LI Qing-qing, JIANG Wen-ming, XU Yuan-cai, YU Ling-hui, NIU Yan-qing, FAN Zi-tian. Development of prominent bonding strength in Al/Mg bimetal composites prepared by ultrasonic vibration-assisted compound casting: Effects of ultrasonic powers [J]. Journal of Materials Science & Technology, 2024, 197: 78−93.

[12] DILIP KUMAR K, SHANTHARAJA M, KUMAR N, MANJUNATHA G. Morphological and mechanical properties of short fibres reinforced hybrid composites for automotive applications [J]. Materials Today: Proceedings, 2022, 52: 957−962.

[13] ONUIKE B, BANDYOPADHYAY A. Functional bimetallic joints of Ti6Al4V to SS410 [J]. Additive Manufacturing, 2020, 31: 100931.

[14] BANAIT S M, PAUL C P, JINOOP A N, KUMAR H, PAWADE R S, BINDRA K S. Experimental investigation on laser directed energy deposition of functionally graded layers of Ni−Cr−B−Si and SS316L [J]. Optics & Laser Technology, 2020, 121: 105787.

[15] KEIST J S, PALMER T A. Role of geometry on properties of additively manufactured Ti−6Al−4V structures fabricated using laser based directed energy deposition [J]. Materials & Design, 2016, 106: 482−494.

[16] LIU Z H, ZHANG D Q, SING S L, CHUA C K, LOH L E. Interfacial characterization of SLM parts in multi-material processing: Metallurgical diffusion between 316L stainless steel and C18400 copper alloy [J]. Materials Characterization, 2014, 94: 116−125.

[17] MEI Xin-liang, WANG Xiang-yu, PENG Yin-bo, GU Hong-yan, ZHONG Gao-yan, YANG Shou-feng. Interfacial characterization and mechanical properties of 316L stainless steel/Inconel 718 manufactured by selective laser melting [J]. Materials Science and Engineering: A, 2019, 758: 185−191.

[18] CHENG Jia-hao, GUSSEV M, ALLEN J, HU Xiao-hua, MOUSTAFA A R, SPLITTER D A, SHYAM A. Deformation and failure of PrintCast A356/316 L composites: Digital image correlation and finite element modeling [J]. Materials & Design, 2020, 195: 109061.

[19] GHASRI-KHOUZANI M, LI X, BOGNO A A, CHEN Z, LIU J, HENEIN H, QURESHI A J. Fabrication of aluminum/stainless steel bimetallic composites through a combination of additive manufacturing and vacuum-assisted melt infiltration casting [J]. Journal of Manufacturing Processes, 2021, 69: 320−330.

[20] ZHANG Ming-yang, YU Qin, LIU Zeng-qian, ZHANG Jian, JIAO Da, LI Shu-jun, PENG Hui, WANG Qiang, ZHANG Zhe-feng, RITCHIE R O. Compressive properties of 3-D printed Mg−NiTi interpenetrating-phase composite: Effects of strain rate and temperature [J]. Composites (Part B): Engineering, 2021, 215: 108783.

[21] CHOE H, SAJI V S, KO Y M. Mechanical properties and corrosion resistance of low rigidity quaternary titanium alloy for biomedical applications [J]. Transactions of Nonferrous Metals Society of China, 2009, 19(4): 862−865.

[22] TAVOOSI M. The Kirkendall void formation in Al/Ti interface during solid-state reactive diffusion between Al and Ti [J]. Surfaces and Interfaces, 2017, 9: 196−200.

[23] ZHAO Yong, WANG Wei-yu, YAN Keng, LIU Chuan, ZOU Jia-sheng. Microstructure and properties of Cu/Ti laser welded joints [J]. Journal of Materials Processing Technology, 2018, 257: 244−249.

[24] HUANG Hao, FU Peng-huai, WANG Ying-xin, PENG Li-ming, JIANG Hai-yan. Effect of pouring and mold temperatures on hot tearing susceptibility of AZ91D and Mg−3Nd−0.2Zn−Zr Mg alloys [J]. Transactions of Nonferrous Metals Society of China, 2014, 24(4): 922−929.

[25] LIU Zhan, NIE Jin-feng, ZHAO Yong-hao. Effect of deformation processing on microstructure evolution and mechanical properties of Mg−Li alloys: A review [J]. Transactions of Nonferrous Metals Society of China, 2024, 34(1): 1−25.

[26] WU Yuan-bing, ZHAO Jian-hua, PENG Wei-li, GU Cheng, CHENG Jin, WANG Ya-jun. Optimization of additive manufactured Ti-based pyramidal lattice structure applied to interface strengthening of Mg/Ti bimetal composites [J]. Transactions of Nonferrous Metals Society of China, 2024,

34(3): 846−860.

[27] GANGIREDDY S, KOMARASAMY M, FAIERSON E J, MISHRA R S. High strain rate mechanical behavior of Ti−6Al−4V octet lattice structures additively manufactured by selective laser melting (SLM) [J]. Materials Science and Engineering: A, 2019, 745: 231−239.

[28] WEN Fu-lin, ZHAO Jian-hua, YUAN Miao-wang, WANG Jing-feng, ZHENG Deng-zhi, ZHANG Jin-yong, HE Ke, SHANGGUAN Jing-jing, GUO Yu. Influence of Ni interlayer on interfacial microstructure and mechanical properties of Ti−6Al−4V/AZ91D bimetals fabricated by a solid–liquid compound casting process [J]. Journal of Magnesium and Alloys, 2021, 9(4): 1382−1395.

[29] MURRAY J L. The Mg−Ti (magnesium-titanium) system [J]. Bulletin of Alloy Phase Diagrams, 1986, 7(3): 245−248.

[30] YAO Fan-jin, YOU Guo-qiang, WANG Lei, LI Qi, ZENG Sheng, MING Yue. Design, fabrication, microstructure, and mechanical properties of interlayer-free vacuum diffusion bonding Mg/Ti composites [J]. Vacuum, 2022, 199: 110947.

[31] DING J J, QIN Q W, HAO S M, WANG X T, CHEN G L. Partial phase diagram of the Ti−Al binary system [J]. Journal of Phase Equilibria, 1996, 17(2): 117−120.

[32] GAO M, WANG Z M, LI X Y, ZENG X Y. Laser keyhole welding of dissimilar Ti−6Al−4V titanium alloy to AZ31B magnesium alloy [J]. Metallurgical and Materials Transactions A, 2012, 43(1): 163−172.

[33] LI Yan-min, YANG Hai-ou, LIN Xin, HUANG Wei-dong, LI Jian-guo, ZHOU Yao-he. The influences of processing parameters on forming characterizations during laser rapid forming [J]. Materials Science and Engineering: A, 2003, 360(1): 18−25.

[34] SIMONELLI M, TSE Y Y, TUCK C. Effect of the build orientation on the mechanical properties and fracture modes of SLM Ti−6Al−4V [J]. Materials Science and Engineering: A, 2014, 616: 1−11.

[35] ZHANG Ming-yang, ZHAO Ning, YU Qin, LIU Zeng-qian, QU Rui-tao, ZHANG Jian, LI Shu-jun, REN De-chun, BERTO F, ZHANG Zhe-feng, RITCHIE R O. On the damage tolerance of 3-D printed Mg−Ti interpenetrating-phase composites with bioinspired architectures [J]. Nature Communications, 2022, 13(1): 3247.

[36] DOROSZKO M, FALKOWSKA A, SEWERYN A. Image-based numerical modeling of the tensile deformation behavior and mechanical properties of additive manufactured Ti−6Al−4V diamond lattice structures [J]. Materials Science and Engineering: A, 2021, 818: 141362.

[37] LIU Yang, XU Huai-zhong, PENG Bin-yi, WANG Xiao-feng, LI Shu-xin, WANG Qun, LI Zhi-guo, WANG Yong-gang. Effect of heating treatment on the microstructural evolution and dynamic tensile properties of Ti−6Al−4V alloy produced by selective laser melting [J]. Journal of Manufacturing Processes, 2022, 74: 244−255.

[38] LIU Lei-feng, DING Qing-qing, ZHONG Yuan, ZOU Ji, WU Jing, CHIU Yu-lung, LI Ji-xue, ZHANG Ze, YU Qian, SHEN Zhi-jian. Dislocation network in additive manufactured steel breaks strength–ductility trade-off [J]. Materials Today, 2018, 21(4): 354−361.

[39] CAO Sheng, CHU Rui-kun, ZHOU Xi-gen, YANG Kun, JIA Qing-bo, SAMUEL LIM C V, HUANG Ai-jun, WU Xin-hua. Role of martensite decomposition in tensile properties of selective laser melted Ti−6Al−4V [J]. Journal of Alloys and Compounds, 2018, 744: 357−363.

[40] FAN Suo, WU He-bao, FANG Jin-xiu. Microstructure and mechanical properties of AZ91D magnesium alloy by expendable pattern shell casting with different mechanical vibration amplitudes and pouring temperatures [J]. China Foundry, 2021, 18(1): 1−8.

[41] WANG X J, WANG N Z, WANG L Y, HU X S, WU K, WANG Y Q, HUANG Y D. Processing, microstructure and mechanical properties of micro-SiC particles reinforced magnesium matrix composites fabricated by stir casting assisted by ultrasonic treatment processing [J]. Materials & Design, 2014, 57: 638−645.

[42] ZHANG Chun-lei, WANG Xiao-jun, WANG Xiao-ming, HU Xiao-shi, WU Kun. Fabrication, microstructure and mechanical properties of Mg matrix composites reinforced by high volume fraction of sphere TC4 particles [J]. Journal of Magnesium and Alloys, 2016, 4(4): 286−294.

[43] OKULOV I V, GESLIN P A, SOLDATOV I V, OVRI H, JOO S H, KATO H. Anomalously low modulus of the interpenetrating-phase composite of Fe and Mg obtained by liquid metal dealloying [J]. Scripta Materialia, 2019, 163: 133−136.

[44] ALGHAMDI A, MACONACHIE T, DOWNING D, BRANDT M, QIAN M, LEARY M. Effect of additive manufactured lattice defects on mechanical properties: An automated method for the enhancement of lattice geometry [J]. The International Journal of Advanced Manufacturing Technology, 2020, 108(3): 957−971.

[45] HEINL P, MÜLLER L, KÖRNER C, SINGER R F, MÜLLER F A. Cellular Ti−6Al−4V structures with interconnected macro porosity for bone implants fabricated by selective electron beam melting [J]. Acta Biomaterialia, 2008, 4(5): 1536−1544.

[46] JIN Nan, WANG Fu-chi, WANG Yang-wei, ZHANG Bo-wen, CHENG Huan-wu, ZHANG Hong-mei. Effect of structural parameters on mechanical properties of Pyramidal Kagome lattice material under impact loading [J]. International Journal of Impact Engineering, 2019, 132: 103313.

[47] YAO Ding-ye, ZHOU Wei-xing, MA Yu-li, HE Bo. Numerical prediction and experimental analysis of the anisotropy of laser powder bed fusion produced Ti−6Al−4V body-centered cubic lattice structure [J]. Journal of Materials Engineering and Performance, 2023, 32(7): 2963−2972.

[48] SCHAEDLER T A, JACOBSEN A J, TORRENTS A, SORENSEN A E, LIAN J, GREER J R, VALDEVIT L, CARTER W B. Ultralight metallic microlattices [J]. Science, 2011, 334(6058): 962−965.

[49] KÖHNEN P, HAASE C, BÜLTMANN J, ZIEGLER S, SCHLEIFENBAUM J H, BLECK W. Mechanical properties and deformation behavior of additively manufactured lattice structures of stainless steel [J]. Materials & Design, 2018, 145: 205−217.

[50] GENG Xiao-liang, LU Ya-hui, LIU Chao, LI Wei-nan, YUE Zhu-feng. Fracture characteristic analysis of cellular lattice structures under tensile load [J]. International Journal of Solids and Structures, 2019, 163: 170−177.

[51] CHATURVEDI V, TALAPANENI T. Effect of mechanical vibration and grain refiner on microstructure and mechanical properties of AZ91Mg alloy during solidification [J]. Journal of Materials Engineering and Performance, 2021, 30(5): 3187−3202.

[52] XU W, BRANDT M, SUN S, ELAMBASSERIL J, LIU Q, LATHAM K, XIA K, QIAN M. Additive manufacturing of strong and ductile Ti−6Al−4V by selective laser melting via in situ martensite decomposition [J]. Acta Materialia, 2015, 85: 74−84.

AZ91D 熔体浸渗 Ti−6Al−4V 金字塔型点阵结构制备 Ti/Mg 双金属复合材料

吴远兵[1]，赵建华[1,2,3]，魏 超[1]，辜 诚[1,2,3]，王亚军[1,2,3]

1. 重庆大学 材料科学与工程学院，重庆 400045；
2. 重庆大学 国家镁合金工程研究中心，重庆 400044；
3. 重庆大学 高端装备铸造技术全国重点实验室，重庆 400044

摘 要：钛合金/镁合金双金属复合材料具有良好的轻量化应用前景。本研究通过 AZ91D 熔体浸渗 Ti−6Al−4V 金字塔型点阵材料制备了 Ti/Mg 双金属复合材料。对比分析了双金属复合材料、Ti−6Al−4V 点阵材料和 AZ91D 基体的拉伸和压缩性能。复合材料的抗拉强度(95.9 MPa)与 Ti−6Al−4V 点阵材料的抗拉强度(94.4 MPa)相当，但低于 AZ91D 的抗拉强度(120.8 MPa)，这归因于双金属界面上的间隙在拉伸过程中阻碍了载荷的传递。复合材料的伸长率为 1.7%，大于 AZ91D 基体的伸长率(1.4%)，但低于 Ti−6Al−4V 点阵材料的伸长率(2.6%)。复合材料的压缩性能优于 Ti−6Al−4V 点阵材料，表明 AZ91D 在压缩变形过程中起到了重要作用。断口分析表明，点阵结构节点处的应力集中导致杆断裂是复合材料和点阵材料的主要失效原因。

关键词：Ti−6Al−4V 点阵结构；Ti−6Al−4V/AZ91D 双金属复合材料；熔体浸渗；力学性能；断口形貌

(Edited by Wei-ping CHEN)